Physical Science

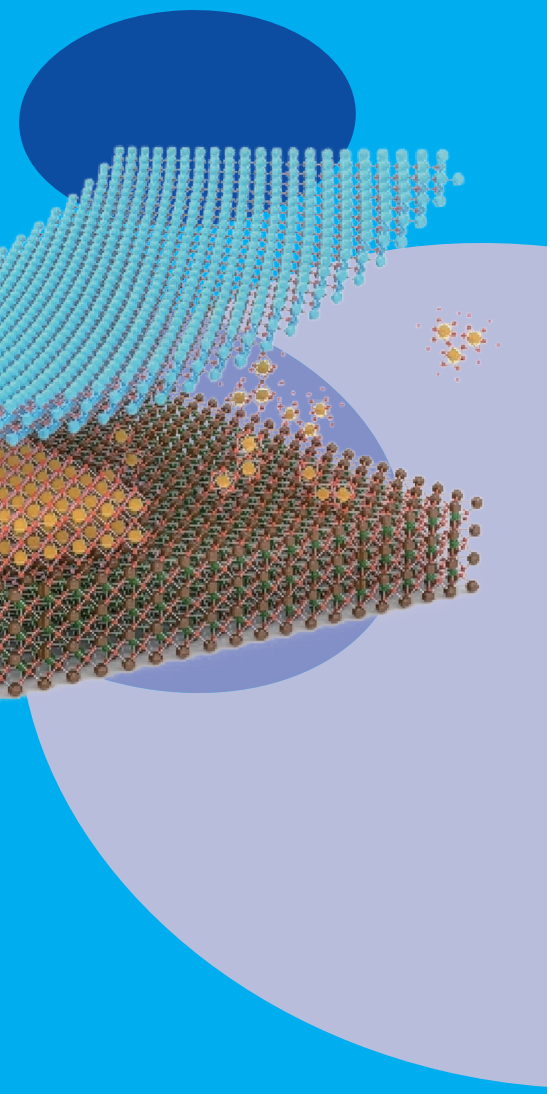

Over the past year, facility users and colleagues have advanced a unified research direction focused on uncovering emergent quantum phenomena and enabling their translation into scalable electronic and spintronic platforms. In correlated quantum materials, spectroscopic and theoretical investigations of the kagome superconductor revealed flat bands pinned near the Fermi level and magnetic excitations evolving across a low-temperature transition, providing rare bulk evidence that flat-band tuning can trigger magnetic ordering. Complementary work on electron-doped cuprates demonstrated a proportional relationship between superconducting transition temperature and the quasiparticle weight of an incipient hole pocket generated by antiferromagnetic spin fluctuations near a quantum critical regime, clarifying the microscopic role of electron–spin interactions in high-T_C superconductivity. Expanding the exploration of emergent magnetism, temperature-dependent angle-resolved photoemission spectroscopy (ARPES) and circular dichroism measurements established high-Curie-temperature spin-valley ferromagnetism in monolayer Cr_2Se_3, identifying valley carrier density as a key factor governing two-dimensional magnetic ordering. In parallel, polarization-dependent hard X-ray photoemission spectroscopy of Co-doped ZnO uncovered a weak donor impurity band crossing the Fermi level, providing direct experimental evidence for the donor-band exchange mechanism responsible for room-temperature ferromagnetism in dilute magnetic semiconductors. Alongside these fundamental discoveries, significant progress was achieved in materials integration and device development. Freestanding ferroelectric membranes were successfully integrated with transition metal dichalcogenides to realize high-κ top-gate dielectrics that enabled sub-60 mV/decade transistors, logic gates, and a 13-nm channel device compatible with semiconductor roadmap targets. Furthermore, stacking-controlled heteroepitaxy of multilayer hexagonal boron nitride on graphene demonstrated moiré-induced polarization and robust, switchable ferroelectricity, establishing a scalable pathway for integrating ferroelectric van der Waals materials. Collectively, these results highlight coherent materials-to-devices progression, linking interaction-driven quantum states, spin-valley and magnetic semiconductors, and ferroelectric two-dimensional electronics. The combined impact lies in strengthening the scientific foundation for next-generation quantum, neuromorphic, and energy-efficient information technologies by bridging fundamental discoveries with scalable device platforms. (by Cheng-Maw Cheng)

Spin Excitations and Flat Electronic Bands in a Kagome Superconductor

A Cr-based kagome system exhibits low-energy magnetic excitations and flat bands close to the Fermi level, suggesting the role of magnetism in its low-temperature emergent properties.

Kagome lattice materials have recently attracted significant attention due to their band structures exhibiting flat bands (FBs) originating from quantum destructive interference of the electronic wave function. In these systems, a tuning of the FB close to the chemical potential can induce electronic instabilities and emergent orders. Extensive experimental studies on kagome lattice materials have shown various types of emergent orders, such as unconventional superconductivity, nematicity, charge density wave (CDW) order, and quantum magnetism. However, these emergent properties have been discussed in relation to characteristic features in the electronic structure, such as Van Hove singularities or Dirac fermions, derived from the inherent topology of the kagome lattice, rather than FBs known in kagome materials. In a major study led by Di-Jing Huang, Qimiao Si, Ming Yi, and Pengcheng Dai, in collaboration with scientists from Taiwan, USA, China, Japan, and Korea, researchers have shown that the low-energy electronic structure of the Cr-based kagome metal superconductor $CsCr_3Sb_5$ is dominated by FBs at the Fermi level (E_F). The researchers observed low-energy magnetic excitations evolving across the low-temperature CDW transition (T_{CDW} = 54 K), suggesting that the low-temperature order has a magnetic origin and that the kagome FBs play a role in the emergence of this order.[1]

The chromium-based kagome metal $CsCr_3Sb_5$ was recently discovered to exhibit a unidirectional CDW order, with superlattice peaks observed by X-ray diffraction (XRD) below T_{CDW} = 54 K. Magnetic susceptibility and nuclear magnetic resonance measurements indicated the simultaneous onset of magnetic order.[2] Band structure calculations revealed multiple competing density wave phases.[3,4] Under hydrostatic pressure, the two orders are separated in temperature and suppressed, and a superconducting dome emerges with a T_C peaking at 6.4 K.[2] Although such a phase diagram resembles those of other unconventional superconducting families, such as the iron-based superconductors and cuprates, the nature of the competing order, as well as evidence of FBs and their association with magnetism across the 54 K CDW phase transition, was not clarified. Using resonant inelastic X-ray scattering (RIXS), angle-resolved photoemission spectroscopy (ARPES), and density functional theory (DFT) calculations, researchers have now shown that the kagome FBs may play an important role in the emergent CDW order.[1]

$CsCr_3Sb_5$ crystallizes in a layered hexagonal lattice consisting of alternatingly stacked Cr–Sb sheets and Cs layers (space group P6/mmm No. 191) with lattice parameters a = 5.4956(1) Å and c = 9.2602(2) Å at 293 K, where the Cr atoms form a kagome lattice (**Fig. 1(a)**).[2] The corresponding 3D BZ is plotted in **Fig. 1(b)**. The authors first characterized the crystal structure at 293 K and then confirmed that superlattice peaks associated with the CDW order set in below T_{CDW}. **Figure 1(c)** shows a map of the reciprocal space in the (H, K, 0) plane where CDW superlattice peaks occurring below T_{CDW} are marked.

The authors carried out RIXS measurements at the Taiwan Photon Source beamline **TPS 41A**. RIXS probes two-particle excitations in momentum transfer q = Δk, such as magnetic excitations, phonons, crystal-field excitations,

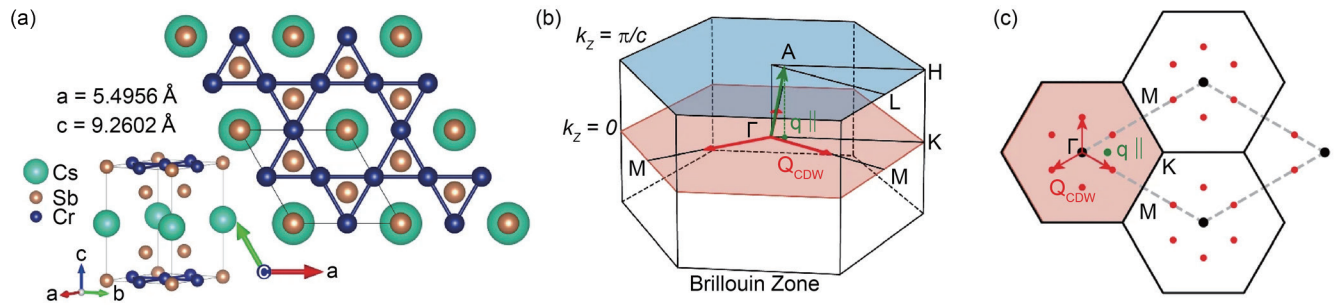

Fig. 1: Crystal structure, Brillouin zone, and CDW order schematics of $CsCr_3Sb_5$. (a) The Cr atoms form a kagome lattice. (b,c) Reciprocal space of $CsCr_3Sb_5$ showing CDW observed by XRD (red arrows or red points). The green arrow marks the q of temperature-dependent RIXS, where q|| is the projection of q onto the sample surface. [Reproduced from Ref. 1]

and plasmons. In particular, it is well-known that magnetic excitations can be conclusively determined when the scattered photons have rotated polarization with respect to the incident beam. **Figure 2(a)** illustrates the scattering geometry of the RIXS experiments carried out by the authors. To conclusively determine spin excitations of the system and exclude other excitations, the authors used π-polarized light with 90° scattering angle between the incident and scattered X-rays of wave vectors k_{in} and k_{out}, respectively. Most importantly, as the dominant low-energy electronic states of $CsCr_3Sb_5$ are derived from Cr 3d orbitals, the authors carried out Cr L_3-edge RIXS to unravel its low-energy excitations. **Figure 2(b)** plots the X-ray absorption spectra across the Cr L_3-edge, and **Fig. 2(c)** plots the RIXS spectra of $CsCr_3Sb_5$ measured at different incident photon energies marked in **Fig. 2(b)**. The 90°-scattering geometry with π-polarized X-rays ensured the measurement of spin excitations and showed a clear spin excitation feature around 70 meV as a shoulder of elastic scattering.

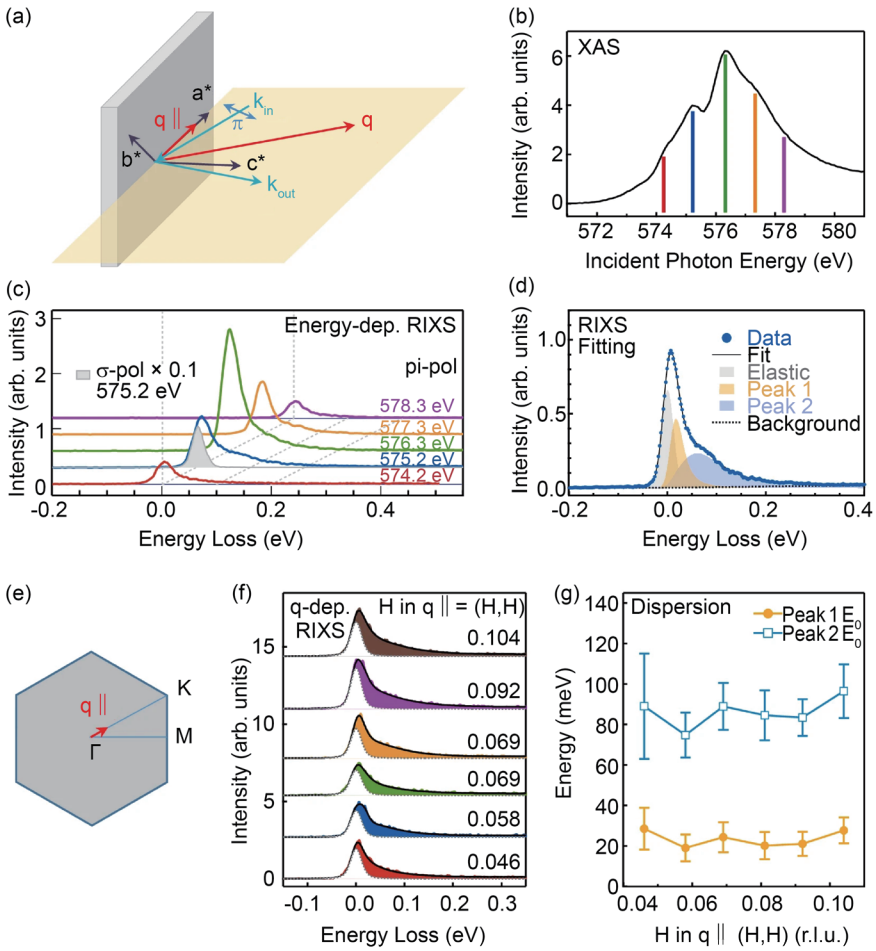

Fig. 2: RIXS measurements. (a) Illustration of RIXS scattering geometry. The scattering plane was perpendicular to the ab plane of $CsCr_3Sb_5$. The incident and scattered wave vectors of X-rays, *i.e.*, k_{in} and k_{out}, are orthogonal. The polarization of incident X-rays was in the scattering plane, *i.e.*, π-polarized, resulting in RIXS with a cross-polarization geometry. The polarization of scattered X-rays was unresolved. The projection of wavevector change q onto the ab plane is denoted as q||. (b) Cr L_3-edge X-ray absorption spectrum of $CsCr_3Sb_5$ recorded at 300 K. Colored vertical bars indicate the X-ray energies used in RIXS measurements. (c) Incident energy–dependent RIXS with q|| along the ΓM direction at 25 K. Spectra in color were recorded with π-polarized X-rays at selected energies. The RIXS spectrum with σ polarization, *i.e.*, X-ray polarization perpendicular to the scattering plane, shows the instrumental energy resolution of RIXS. (d) Curve fitting for measured RIXS spectra was performed using a linear background and a spectral profile consisting of three components: one elastic and two electronic excitations. (e) First Brillouin zone in the a*b* plane of reciprocal space. The red arrow indicates q|| of momentum-dependent RIXS measurements. (f) Momentum-dependent RIXS with q|| along ΓK at 25 K. The energy of incident photons was set to 575.2 eV to optimize the shoulder feature. The dashed lines plot the elastic components; the colored shades indicate spectral profiles arising from spin excitations. (g) Dispersion of fitted undamped energy E_0 of two spin excitations as a function of in-plane momentum q||. [Reproduced from Ref. 1]

The measured RIXS spectrum was fitted to a spectral profile comprising three components: one elastic peak, two electronic excitations, and a polynomial background, as shown in **Fig. 2(d)**. The authors also measured momentum-dependent RIXS with q|| along Γ– K (**Fig. 2(e)**) to further verify that the observed electronic excitations arise from transitions involving FBs. **Figure 2(f)** summarizes the q|| dependence of the magnetic excitations within the available momentum transfer range along the [H, H, 0] direction. The fitted undamped energy E_0 of the two spin components in the RIXS data shows no dispersion for all q|| within the available range, as plotted in **Fig. 2(g)**, indicating direct evidence of FBs. This is consistent with the FB results obtained from ARPES measurements as discussed below.

The authors conducted a comparison of the temperature dependence of the FBs and spin excitations across T_{CDW} using ARPES and RIXS. **Figure 3(a)** shows the ARPES band dispersion map along Γ–M taken with linear vertical (LV) polarization at 10 K (left) and 140 K (right), suitable for selecting the FB of d_{yz} orbital. The FBs are visible at both temperatures, as seen in the map, the peak in the Energy Distribution Curve (EDC) (**Fig. 3(b)**), and the bend in the fitted band dispersion (marked by a white and red arrow, respectively). From the map, the FB location appears closer to E_F at 140 K compared to 10 K. This is seen more clearly in the direct comparison of the EDC (**Figs. 3(b) and 3(c)**) taken at the location marked by the black arrow: the peak is shifted towards E_F at 140 K by about 20 meV, and is recovered after thermally cycling back to

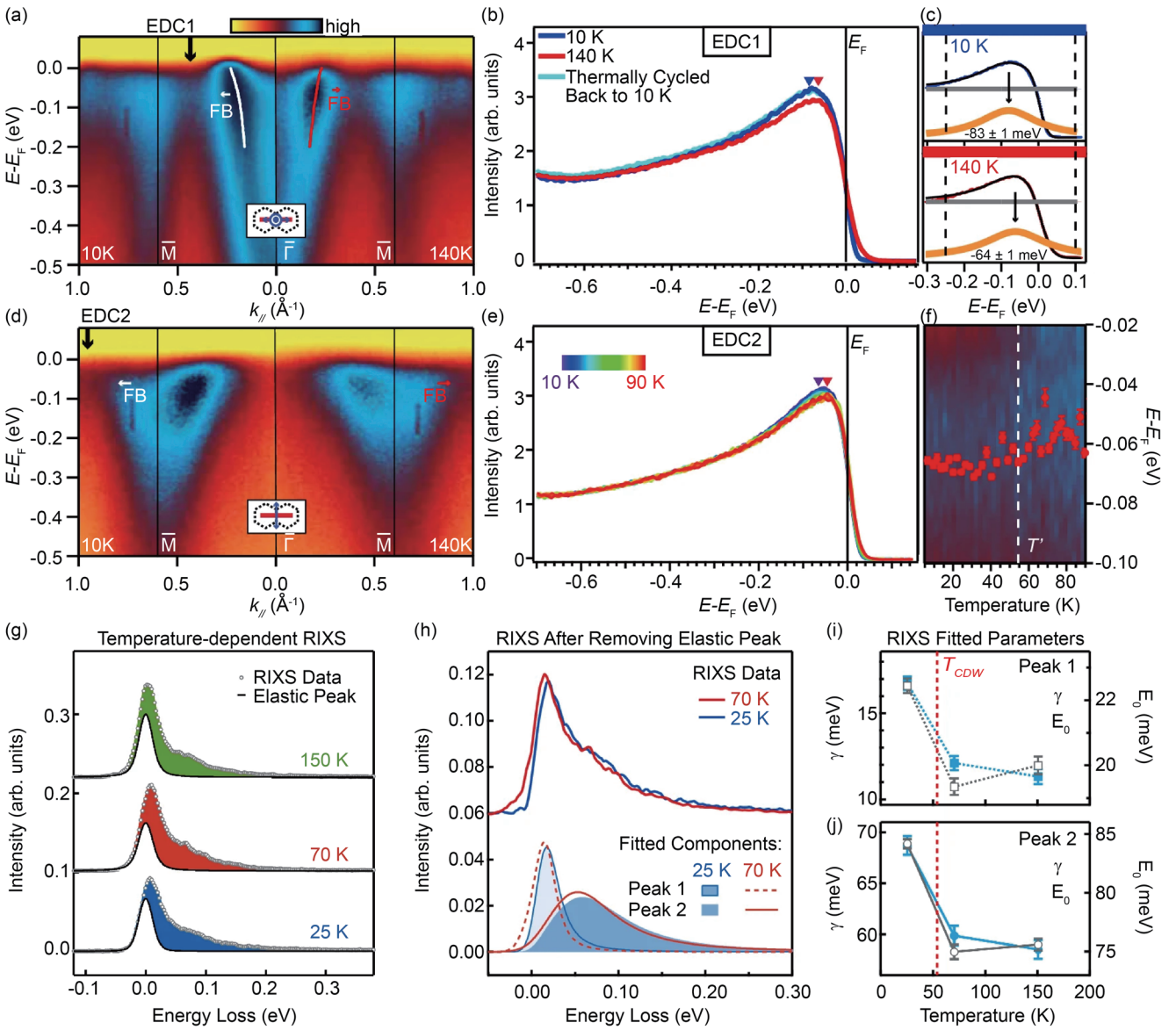

Fig. 3: Temperature-dependent results of ARPES and RIXS. (a) Band dispersion obtained with 114 eV LH polarization and horizontal slit direction at 10 K (left) and 140 K (right). White (10 K) and red (140 K) dots denote the fitted momentum distribution curve positions for the electron pocket at Γ. The arrows mark a kink in the dispersion, indicating hybridization with the FB. (b) EDC1 measured at position marked in (a) at 10 K, 140 K, and thermally cycled back to 10 K. (c) Fitting at 10 K and 140 K for EDC1 showing a Lorentzian peak (orange) with constant background (gray), multiplied by the Fermi–Dirac (FD) function convolved with a Gaussian peak of 40 meV full width at half maximum (FWHM) for experimental resolution. Blue/red dots are the raw data points, the same as (b). Vertical dashed lines mark the fitting range. The dashed arrows denote the fitted Lorentzian peak positions. (d) Same as (a) but measured with LV polarization. (e) EDC2 as marked in (d) measured from 10 K to 90 K. (f) Fitted FB positions from EDCs after dividing the FD function convolved with a Gaussian peak with 40 meV FWHM. The dotted line marks the transition T_{CDW}. (g) Temperature-dependent RIXS. Open circles depict raw RIXS data measured with π-polarized incident X-rays at an energy of 572.5 eV and temperatures of 25, 70, and 150 K; solid lines plot the fitted elastic components. The shaded areas denote RIXS features arising from spin excitations. (h) RIXS spectra at 25 K (blue) and 70 K (red) after removing the elastic component. The bottom panel compares the fitted components of spin excitations. (i,j) Evolution of fitted parameters E_0 and γ for temperatures across T_{CDW} (vertical dashed line). [Reproduced from Ref. 1]

10 K. Similarly, the comparison of band dispersion along Γ–M taken with linear horizontal (LH) polarization and horizontal slit at 10 K ($T < T_{CDW}$) and 140 K ($T > T_{CDW}$) shows that FB of d_{xz} orbital also shift towards E_F (**Figs. 3(d) and 3(e)**). The authors plotted the continuous temperature evolution of this shift, as presented in **Fig. 3(f)**. They also conducted temperature-dependent RIXS measurements at temperatures across T_{CDW}. **Figure 3(g)** presents the measured RIXS spectra within an energy range of 0.3 eV. All spectra were analyzed using the same curve-fitting scheme as shown in **Fig. 2(d)**. To highlight the spectral changes, **Fig. 3(h)** compares RIXS spectra above and below T_{CDW} after removing elastic scattering, revealing a subtle but distinct broadening and shift toward higher energy as the temperature is cooled across T_{CDW}. For quantitative analysis, **Figs. 3(i) and 3(j)** show the evolution of the fitted bare energy E_0 and damping factor γ of both spin excitations, consistent with ARPES results shown in **Fig. 3(f)**.[4] The observed excitations are coupled to the electron–hole excitations across E_F. Thus, the broadening and shifting of

the spin excitations likely reflect the shifting of the FBs away from E_F, both below and above E_F.[1]

Finally, the authors discuss that while their bare DFT electronic structure calculations do not accurately reproduce the observed bands below E_F, but when the necessary correlation corrections reconciles the discrepancies in the FB position at a qualitative level. This confirms the potential mechanism for the involvement of the kagome FBs in the formation of the CDW electronic order. Furthermore, since the chemical potential of $CsCr_3Sb_5$ is close to the kagome FBs, it is conceivable that their presence drives an electronic order that pushes the FBs away from the E_F, as observed in experiments. With hydrostatic pressure, this electronic CDW order can get suppressed and leave residual density of states from the FBs near E_F to experience the quantum fluctuations expected near a quantum critical point and potentially enable superconductivity. The authors conclude that the flat band in $CsCr_3Sb_5$ is clearly participates in the low-temperature order, as is evident from its shift away from E_F and its coupling with spin excitations.[1] (Reported by Ashish Chainani)

This report features the work of Di-Jing Huang, Qimiao Si, Ming Yi, Pengcheng Dai and their collaborators published in Nat. Commun. ***16****, 7573 (2025).*

TPS 41A Soft X-ray Scattering

- RIXS
- Materials Science, Condensed-matter Physics

References

1. Z. Wang, Y. Guo, H.-Y. Huang, F. Xie, Y. Huang, B. Gao, J. S. Oh, H. Wu, J. Okamoto, G. Channagowdra, C.-T. Chen, F. Ye, X. Lu, Z. Liu, Z. Ren, Y. Fang, Y. Wang, A. Biswas, Y. Zhang, Z. Yue, C. Hu, C. Jozwiak, A. Bostwick, E. Rotenberg, M. Hashimoto, D. Lu, J. Kono, J.-H. Chu, B. I. Yakobson, R. J. Birgeneau, G.-H. Cao, A. Fujimori, D.-J. Huang, Q. Si, M. Yi, P. Dai, Spin excitations and at electronic bands in a Cr-based kagome superconductor, Nat. Commun. **16**, 7573 (2025).
2. Y. Liu, Z.-Y. Liu, J.-K. Bao, P.-T. Yang, L.-W. Ji, S.-Q. Wu, Q.-X. Shen, J. Luo, J. Yang, J.-Y. Liu, C.-C. Xu, W.-Z. Yang, W.-L. Chai, J.-Y. Lu, C.-C. Liu, B.-S. Wang, H. Jiang, Q. Tao, Z. Ren, X.-F. Xu, C. Cao, Z.-A. Xu, R. Zhou, J.-G. Cheng, G.-H. Cao, Nature **632**, 1032 (2024).
3. C. Xu, S. Wu, G.-X. Zhi, G. Cao, J. Dai, C. Cao, X. Wang, H.-Q. Lin, Nat. Commun. **16**, 3114 (2025).
4. S. Wu, C. Xu, X. Wang, H.-Q. Lin, C. Cao, G.-H. Cao, Nat. Commun. **16**, 1375 (2025).

How Antiferromagnetism Shapes Superconductivity in Cuprate Materials

Their remarkable work links hidden magnetism to the birth of superconductivity in complex quantum materials.

Superconductivity in cuprates has remained a central challenge for more than four decades. Despite the discovery of numerous competing and intertwined phases, one of the most robust and universal features of the cuprate phase diagram is the dome-shaped T_C that arises near the boundary of antiferromagnetic (AF) order. This proximity has long suggested that AF spin fluctuations may serve as the pairing mechanism for superconductivity. Theoretical studies have explained the unconventional d-wave pairing symmetry within this framework, while angle-resolved photoemission spectroscopy (ARPES) has provided direct experimental access to quasiparticles and their many-body renormalization effects. However, determining how AF spin fluctuations specifically affect electronic states and promote superconductivity remains challenging due to strong correlations and the complexity of the cuprate phase diagram.

In the presence of long-range AF order at low electron doping, a superlattice potential folds the electronic bands and reconstructs the Fermi surface from a large hole-like cylinder into smaller electron and hole pockets. While this folding is well understood within mean-field descriptions of long-range AF order, remnants of reconstructed pockets have also been observed in the superconducting regime beyond the long-range AF phase boundary. These observations suggest a role for short-range AF fluctuations or other ordering phenomena. Further complicating the interpretation, ARPES studies have reported the simultaneous presence of both folded AF bands and unfolded pristine bands, indicating strong electron correlations and challenging conventional models.

Transport measurements have provided further evidence linking superconductivity to one of the AF-induced Fermi pockets. Magnetoresistance and quantum oscillation experiments on electron-doped cuprates such as $Nd_{2-x}Ce_xCuO_4\pm\delta$ have shown that hole-pocket contributions to conductivity occur only within the superconducting doping range. However, because these measurements require strong magnetic fields, it remains unclear whether the hole pocket is intrinsically associated with superconductivity under ambient conditions or if it is stabilized by field-enhanced AF order.

To resolve this issue, Changyoung Kim and his team at Seoul National University, Korea, combine ARPES and zero-field muon spin rotation/relaxation (μSR) measurements on the electron-doped cuprate Pr_{1-x} $LaCe_xCuO_4\pm\delta$ (PLCCO). This work is complemented by Hubbard-model calculations using cluster perturbation theory. Doping-dependent ARPES measurements were conducted at the **TPS 39A** nanoARPES beamline, focusing on the low-energy quasiparticle states along the nodal direction (nodal band) after removing the Fermi–Dirac cutoff, as shown in **Fig. 1**. The most underdoped non-superconducting sample (n ≈ 0.06) shows a clear energy gap that gradually closes with increasing electron doping. Within a mean-field framework, this gap originates from quasiparticle band splitting induced by effective AF scattering with Q = (π, π), and its closure reflects the weakening of the AF superlattice potential.

Although AF band folding is expected, the folded branch is barely visible in raw spectra due to weak matrix-element effects. In heavily underdoped samples (n ≈ 0.06 and 0.11), the shadow AF branch becomes discernible through stacked and normalized energy distribution curves, revealing a flattened band top and back-bending behavior centered at the AF zone boundary. As doping increases, the AF branch becomes diffuse and ill-defined, accompanied by spectral broadening and enhanced in-gap spectral weight. This enhancement is attributed to the growth of unfolded pristine states. The simultaneous presence of folded AF features and in-gap intensity indicates a superposed Fermi surface consisting of AF-derived pockets and a large pristine Fermi surface, reflecting many-body effects that extend beyond the conventional mean-field description. In addition to the phenomenological analysis, the researchers conducted a function-fit analysis on the nodal band spectra

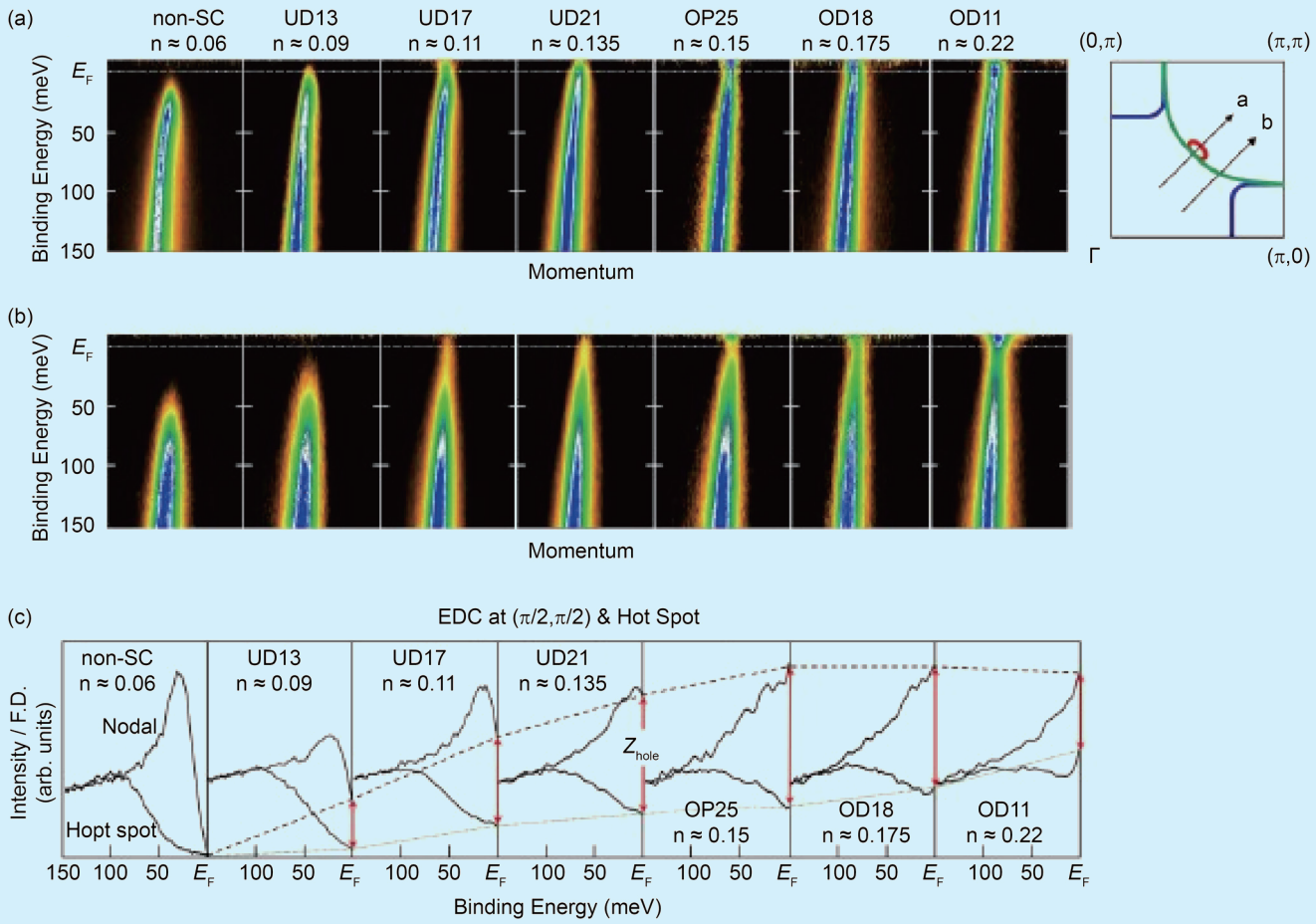

Fig. 1: Doping evolution of the nodal band in PLCCO. ARPES spectra collected along the nodal line. ARPES spectra collected along the hot spot. Energy Distribution Curves (EDCs) at (π/2, π/2) and the hot-spot point for various doping levels. Black dashed and green dotted lines indicate the zero-energy intensity of each EDC. [Reproduced from Ref. 1]

without involving the hot-spot spectra. The function fitting also allows them to determine the AF peak position even in the overdoping region where the peak shape is ambiguous due to strong in-gap pristine intensity. They reported the unconventional reconstruction of the Fermi surface, characterized by the coexisting L-circle and pockets, originates from strong correlations instead of static disorder.

Their high-resolution ARPES shows that the nodal quasiparticle spectrum contains both folded AF and unfolded pristine components, consistent with numerical simulations. By monitoring the doping evolution of the folded AF branch, the study finds that superconductivity appears when the folded hole band first crosses the Fermi energy within a short-range AF ground state, near a possible quantum critical point separating static and dynamic AF order. Notably, the zero-energy spectral weight of the hole band scales with T_C, while the energy difference between the band top and the Fermi level is inversely correlated with T_C. These findings indicate that an incipient hole band, driven by electron–spin fluctuation coupling, plays a central role in the emergence of superconductivity in electron-doped cuprates. (Reported by Cheng-Maw Cheng)

This report features the work of Changyoung Kim and his collaborators published in Nat. Commun. ***16****, 2764 (2025).*

TPS 39A Nanometer Angle-resolved Photoemission Spectroscopy (NanoARPES)

- Angle-resolved Photoemission Spectroscopy
- Materials Science, Condensed-matter Physics

Reference

1. D. Song, S. Lee, Z. Shen, W. Jung, W. Lee, S. Choi, W. Kyung, S. Jung, C.-M. Cheng, J. Kwon, S. Ishida, Y. Yoshida, S. R. Park, H. Eisaki, Y. Wang, K.-Y. Choi, C. Kim, Nat. Commun. **16**, 2764 (2025).

Spin-Valley Coupling Enhanced High-T_C Ferromagnetism in a Non-van der Waals Monolayer Cr_2Se_3 on Graphene

Metallic ferromagnetism with a record high Curie temperature (T_C ~225 K) originating from spontaneous spin-valley polarization is reported for a binary monolayer: Cr_2Se_3 on graphene.

Spin-valley coupled magnetic ordering is known to occur in layered van der Waals transition-metal dichalcogenides, but with ordering temperatures below 55 K. Recent theoretical studies predicted that non-van der Waals structures can also exhibit spin-valley polarization–induced semiconducting ferromagnetic (FM) ground states, but experimental confirmation was lacking. In an international collaboration between Japan, France, and Taiwan, researchers have now reported a record high Curie temperature (T_C ~ 225 K) metallic ferromagnetism arising from spontaneous spin-valley polarization in the non-van der Waals monolayer (ML) of the binary compound Cr_2Se_3 on graphene. Using angle-resolved photoemission spectroscopy (ARPES), X-ray absorption spectroscopy (XAS), X-ray magnetic circular dichroism (XMCD), and circular dichroism (CD) in ARPES, Chien-Wen Chuang (Tohoku University), Takafumi Sato (Tohoku University), Ashish Chainani (NSRRC) and their collaborators have demonstrated that ML Cr_2Se_3 on graphene exhibits spin-valley-coupled FM ordering.[1]

A recent first-principles calculation predicted that a combination of broken inversion symmetry, strong spin-orbit coupling, and magnetic exchange interaction with intrinsic out-of-plane magnetization in ML Cr_2Se_3 results in a spontaneous coupling of spin and valley polarization. This leads to a FM semiconductor with anomalous valley Hall effect.[2] However, there have been no experimental reports of spin-valley coupling in either bulk or ML Cr_2Se_3, or in any non-van der Waals material. Furthermore, there is no experimental evidence that magnetic ordering temperatures are enhanced or exceed 55 K due to spin-valley coupling.[3]

Cr_2Se_3 is a non-van der Waals material, and its ML consists of a quintuple set of Se-Cr-Se-Cr-Se atomic layers, as shown in **Fig. 1(a)**. The authors used molecular beam epitaxy to grow 1 to 3 MLs of Cr_2Se_3 on graphene. The reflection high-energy electron diffraction (RHEED) pattern of the fabricated film showed clear streaks associated with the 1 × 1 structure of Cr_2Se_3, besides the 1 × 1

pattern from the 2 ML graphene (**Fig. 1(b)**). The estimated in-plane lattice constant (3.6 Å) supports the formation of the Cr_2Se_3 phase, which was directly confirmed by transmission electron microscopy measurements. The low-energy electron diffraction (LEED) pattern showed sharp six-fold 1 × 1 spots originating from the Cr_2Se_3 films, alongside the 1 × 1 spots of graphene (**Fig. 1(c)**), indicating its high-quality single crystallinity. Soft X-ray photoemission spectroscopy revealed Cr^{3+} features, further supporting the formation of the Cr_2Se_3 phase. To clarify ferromagnetism, temperature(T)-dependent XAS-XMCD measurements of the Cr L-edge (2p–3d) were conducted at the **TLS 11A1** Dragon beamline. The XAS spectrum of 1 ML Cr_2Se_3 at T = 70 K, for both positive and negative out-of-plane magnetic fields (± 1.0 T), showed Cr L_3 and L_2 main peaks at $h\nu$ ~ 577 eV and 585 eV (**Fig. 1(d)**), respectively. The XAS difference spectrum between the +1.0 T and −1.0 T spectra exhibited small but clear features and indicated a finite XMCD, thus proving FM ordering. The authors then performed charge-transfer cluster model spectral calculations, which reproduced the experimental XAS and XMCD spectra (**Fig. 1(d)**). The resulting electronic parameters indicated that 1 ML Cr_2Se_3 is a negative-charge transfer material with a Cr^{3+} $t_{2g}^{3\uparrow}$ electron configuration and a magnetic moment of 3.4 μB per Cr atom. These results establish that 2D magnetism is realized in the non-van der Waals type 1 ML Cr_2Se_3 material.[1]

To estimate T_C from magnetization-sensitive measurements, the authors performed T-dependent XMCD measurements in the total electron yield mode. **Figure 2(a)** shows T-dependent XMCD intensity for 1 ML Cr_2Se_3 at the Cr L_3 and L_2 edges for T = 70, 180, 225, and 250 K. The XMCD intensity systematically reduced from T = 70 K to 225 K, and by T = 250 K, the XMCD signal had vanished. Similarly, the XMCD intensity for 3 ML Cr_2Se_3 at T = 70, 125, 150, and 175 K, as shown in **Fig. 2(b)**, signifies a finite XMCD intensity up to T = 150 K but became negligible at T = 175 K. The XMCD intensity at the L_3 peak ($h\nu$ = 577.0 eV) plotted vs. T in **Fig. 2(c)** suggests that the T_C value from the XMCD measurements is 225–250 K and 150-175 K for 1 and 3 ML, respectively.

The authors also employed T-dependent ARPES with circularly polarized photons to study the relationship between band dispersions and FM ordering, as shown in **Figs. 3(a)–3(c)** on the next page. The results showed that localized Cr $3d^{\uparrow}$-t_{2g} bands exhibit systematic energy shifts and band splitting of spectral features at the Γ, K, and K' points at high binding energies (E_B), and occupancy of the itinerant Cr 3d–e_g valleys at the K and K' points near the Fermi level (E_F). As shown in **Fig. 3(d)**, at the Γ point, a main peak is observed at E_B = 2.16 eV with a shoulder at 2.36 eV at T = 40 K, indicating the existence of a double

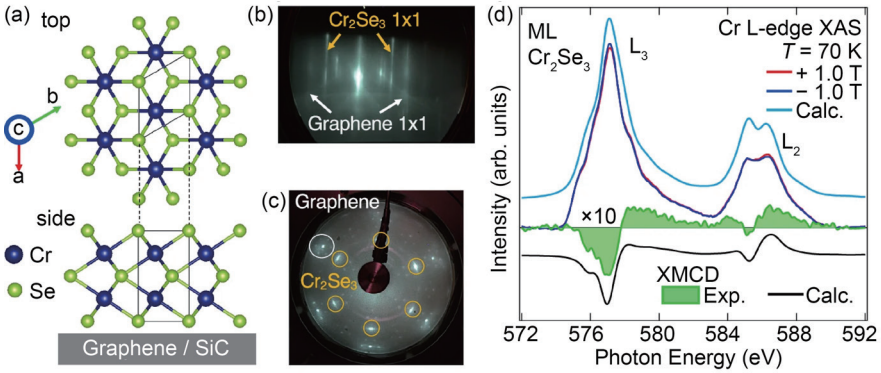

Fig. 1: Fabrication and characterization of ML Cr_2Se_3 film. (a) Top and side views of the crystal structure (P6-m2 space group) of ML Cr_2Se_3 on 2 ML graphene/SiC (0001). Black rectangles indicate the unit cell, which consists of quintuple layers with a Se-Cr-Se-Cr-Se stacking sequence. (b) RHEED pattern of ML Cr_2Se_3. White and yellow arrows indicate the 1 × 1 patterns from graphene and Cr_2Se_3, respectively. (c) LEED pattern of ML Cr_2Se_3 measured with a primary electron energy of 90 eV. Yellow and white circles represent the 1 × 1 spots from Cr_2Se_3 and graphene, respectively. (d) Cr L edge (2p–3d) XAS spectrum of ML Cr_2Se_3 measured with an applied magnetic field of ±1.0 Tesla (T) at 70 K (red and blue curves). The green area shows the difference between +1.0 T and −1.0 T data, expanded vertically by a factor of 10, corresponding to the experimental XMCD. Numerical simulations based on the charge transfer cluster model for XAS and XMCD spectra are shown with light blue and black curves, respectively. [Reproduced from Ref. 1]

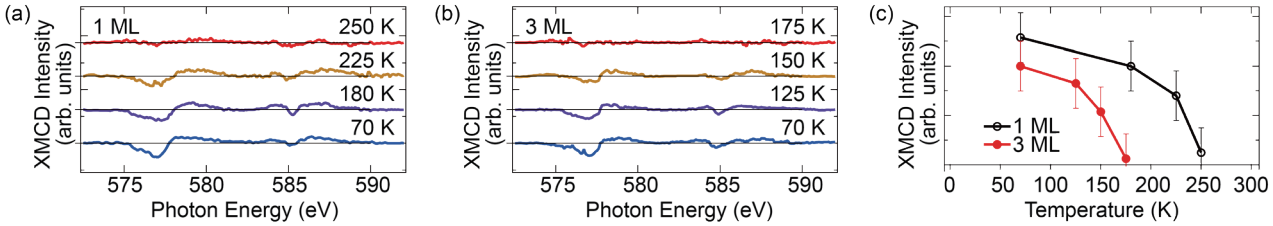

Fig. 2: Determination of T_C by XMCD measurements. (a,b) Temperature dependence of the XMCD signal at the Cr L_3 and L_2 edges for 1 ML and 3 MLs, respectively. (c) Plot of XMCD intensity at the L_3 peak ($h\nu$ = 577.0 eV) versus temperature for 1 ML and 3 MLs, showing a reduction of T_C with increasing number of layers. [Reproduced from Ref. 1]

peak (p1 and p2 in **Fig. 3(d)**). Similar band splitting was also observed at the K/K' point, as shown for the K' point in **Fig. 3(e)**. These band splittings of Cr–Se hybridized states disappear between T = 225–250 K (**Figs. 3(d) and 3(e)**), consistent with T_C ~225 K for 1 ML Cr_2Se_3 estimated from XAS-XMCD (**Fig. 2(a)**).

Evidence for CD in the occupied $t_{2g}{}^{\uparrow}$ bands at the K and K' points at 40 K for ML Cr_2Se_3 was observed, as shown in **Fig. 3(f)**. Using right and left circularly polarized light (C+ and C-), the energy distribution curves (EDCs) obtained at the K point (red and pink curves) showed a difference in peak intensity, indicating finite CD. This CD was also observed at the K' point (blue and light blue curves), but with a sign reversal compared to the K point, as shown by the vertically expanded subtracted EDCs (yellow and purple curves). A sign reversal of CD was also found for the $e_g{}^{\uparrow}$ pockets between the K and K' points (see inset to **Fig. 3(f)**). Notably, the sign is reversed between the $t_{2g}{}^{\uparrow}$ and $e_g{}^{\uparrow}$ bands. These results suggest that photoelectron excitations are asymmetric between the K and K' points, indicating valley-selective CD, *i.e.*, spin-valley polarization. Consequently, the t_{2g}–e_g spin-valley coupling at the K/K' points of the hexagonal Brillouin zone leads to spontaneous FM ordering. The CD observed in ARPES also provided clear evidence of magnetically sensitive spin-valley polarized states.[1]

Finally, the authors confirmed that the reduction of T_C with an increasing number of layers is caused by a decrease in the electron carrier density transferred from the substrate across the Cr_2Se_3:graphene interface. The XAC-XMCD and ARPES results indicate that T_C is proportional to the carrier density (which correlates with the measured spectral density of states at E_F). The results suggest that ferromagnetism is likely due to the localized t_{2g} spins coupled *via* the Ruderman-Kittel-Kasuya-Yosida (RKKY) interaction active in the valley e_g-electron pockets of Cr_2Se_3 films grown on graphene. (Reported by Ashish Chainani)

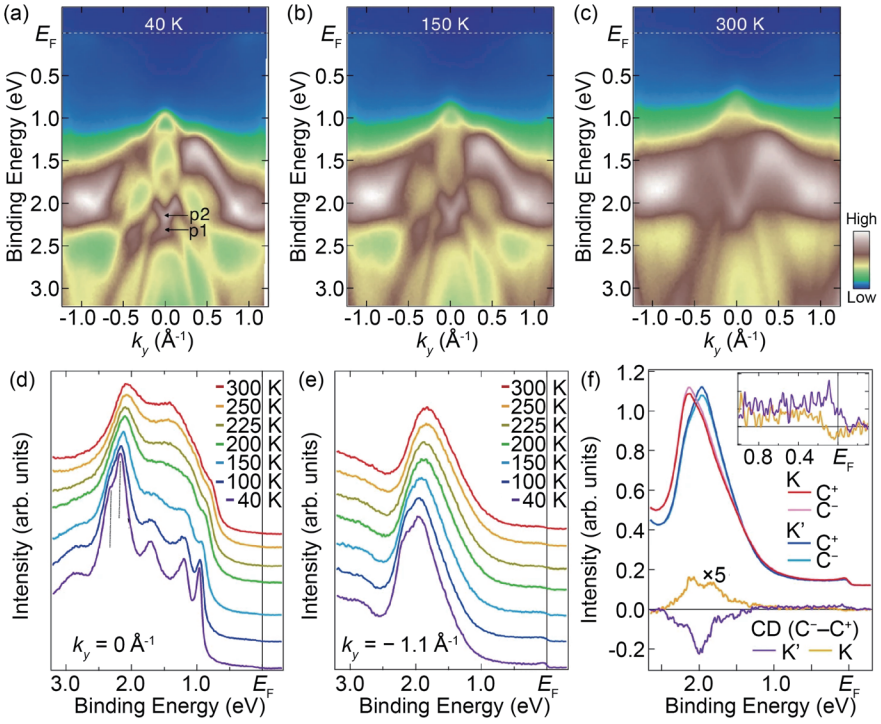

Fig. 3: Temperature evolution of band structure and evidence for spin-valley polarization. (a–c) ARPES intensity plots along the ΓK cut measured at T = 40, 150, and 300 K, respectively, using circularly polarized photons of $h\nu$ = 75 eV. Peaks p1 and p2 are also indicated. (d,e) Temperature dependence of EDCs at selected k cuts along k_y = 0.0 (Γ) − 1.1 Å^{-1} (K'), respectively. (f) EDCs for ML Cr_2Se_3, obtained at the K and K' points with C+ and C- polarized lights using $h\nu$ = 75 eV. Yellow and purple curves represent subtracted EDCs obtained with C+ and C- photons expanded vertically by 5 times. The inset shows the expansion near E_F. A clear CD associated with spin-valley polarization reverses its sign between the K and K' points. [Reproduced from Ref. 1]

This report features the work of Chien-Wen Chuang, Takafumi Sato, Ashish Chainani and their collaborators published in Nat. Commun. ***16****, 3448 (2025).*

TLS 11A1 (Dragon) MCD, XAS

- XAS-XMCD
- Materials Science, Condensed-matter Physics

References

1. C.-W. Chuang, T. Kawakami, K. Sugawara, K. Nakayama, S. Souma, M. Kitamura, K. Amemiya, K. Horiba, H. Kumigashira, G. Kremer, Y. Fagot-Revurat, D. Malterre, C. Bigi, F. Bertran, F. H. Chang, H. J. Lin, C. T. Chen, T. Takahashi, A. Chainani, T. Sato, Nature Comm. **16**, 3448 (2025).
2. Z. He, R. Peng, X. Feng, X. Xu, Y. Dai, B. Huang, Y. Ma, Phys. Rev. B. **104**, 075105 (2021).
3. B. Edwards, O. Dowinton, A. E. Hall, P. A. E. Murgatroyd, S. Buchberger, T. Antonelli, G.-R. Siemann, A. Rajan, E. Abarca Morales, A. Zivanovic, C. Bigi, R. V. Belosludov, C. M. Polley, D. Carbone, D. A. Mayoh, G. Balakrishnan, M. S. Bahramy, P. D. C. King , Nat. Mater. **22**, 459 (2023).

When Two-Dimensional Crystals Learn to Remember

This work enables scalable, switchable atomic ferroelectrics, paving the way for ultra-thin, low-power, nonvolatile future electronics.

Two-dimensional (2D) ferroelectrics, which maintain electric polarization at atomic-layer thicknesses, hold significant potential for next-generation electronic devices beyond Moore's law, enabling efficient energy storage and high-density information processing. In naturally occurring van der Waals crystals such as hexagonal boron nitride (h-BN) and transition-metal dichalcogenides, ferroelectricity is absent because these materials favor centrosymmetric stacking configurations with lower formation energy. This limitation was addressed by mechanically exfoliating and restacking h-BN layers with controlled rotational and translational offsets, thereby breaking inversion symmetry and inducing out-of-plane polarization. The discovery of ferroelectricity in twisted h-BN has sparked broad interest in symmetry-breaking phenomena, including giant piezoelectricity and ferroelectricity in other layered materials. For practical device applications, scalable and controllable synthesis of ferroelectric h-BN is crucial.

Chemical vapor deposition (CVD) is a promising bottom-up method for producing large-area, high-quality h-BN films and is widely used for 2D dielectrics. However, epitaxial growth of multilayer h-BN with polarized stacking on inert or non-metal substrates remains highly challenging, as CVD growth typically favors non-polar configurations and lacks catalytic support after monolayer formation.

Unlike CVD, which relies on substrate catalysis, molecular beam epitaxy (MBE) is well suited for the controlled growth of multilayer structures due to its precise flux control and *in situ* reflection high-energy electron diffraction (RHEED) monitoring. In this work, Chung-Lin Wu (National Cheng Kung University), Cheng-Maw Cheng (NSRRC), and their teams used the nitrogen plasma-assisted MBE (PA-MBE) method to directly grow layer-controlled hexagonal boron nitride (h-BN) on lattice-matched graphene formed on

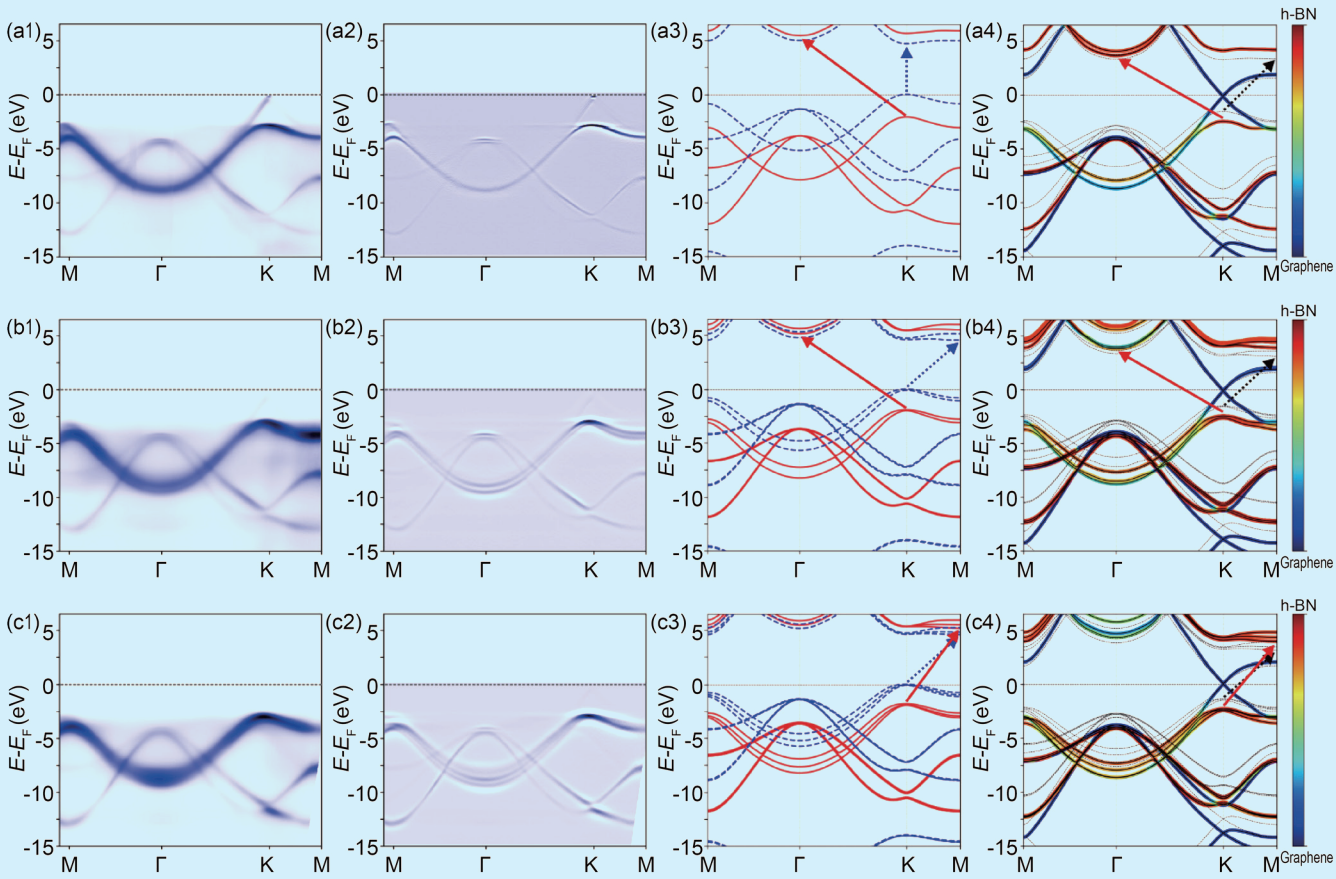

Fig. 1: Electronic band structures of h-BN and h-BN/graphene. (a1–c1) ARPES spectra of mono-, bi- and tri-layer h-BN/graphene. (a2–c2) The corresponding 2nd derivatives of ARPES data in (a1–c1). (a3–c3) Electronic band structures of free-standing mono-, bi-, and tri-layer h-BN calculated at the density function theory (blue dashed curves) and GW (red solid curves) levels. (a4–c4) Orbital-projected GW band structures for h-BN (red) and graphene (blue) lateral heterostructures. [Reproduced from Ref. 1]

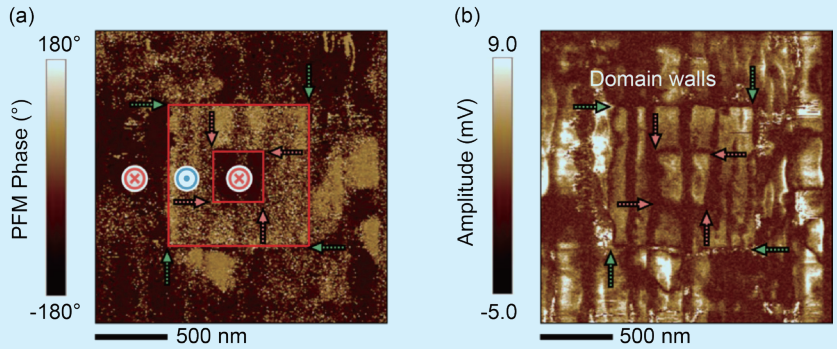

Fig. 2: Box-in-box pattern (+5 V/1000×1000 nm², −6 V/400×400 nm²) on 3 MLs h-BN sample. (a) Phase and (b) amplitude images of the box-in-box pattern on a 3 ML h-BN sample. [Reproduced from Ref. 1]

a commercially available 4H-SiC (0001) substrate with a 4° miscut. After ultra-high-vacuum annealing, high-quality multilayer graphene with step edges along the $\langle 1\bar{1}20 \rangle$ direction was epitaxially grown, as confirmed by streak RHEED patterns. Under nitrogen-rich conditions, N_2 plasma enhances boron surface diffusion, enabling h-BN growth at temperatures significantly lower than those required for CVD. Scanning probe and electron microscopy reveal smooth, continuous monolayer h-BN covering atomically flat graphene terraces and extending across step edges. Preferential nucleation at step edges promotes aligned bilayer island growth and seamless island merging, resulting in high-quality layer-by-layer h-BN films. Raman spectroscopy further confirms the exceptional crystalline quality of the grown h-BN.

To deepen the understanding of the stacked sequence, they performed angle-resolved photoemission spectroscopy (ARPES) at the **TLS 21B1** high-resolution photoemission spectroscopy beamline. The high crystalline quality and uniform stacking order of the layer-controlled h-BN films are confirmed by the excellent agreement between ARPES measurements and layer- and stacking-dependent GW band-structure calculations. The chemically inert nature of MBE-grown h-BN enables reliable *ex situ* ARPES measurements without protective capping layers. ARPES spectra of mono-, bi-, and trilayer h-BN along high-symmetry directions in the Brillouin zone reveal clear layer-dependent band dispersions. Although graphene π bands from the underlying substrate contribute to the spectra, characteristic features such as band splitting near the K point confirm the Bernal stacking of multilayer graphene. Distinct parabolic dispersions appear in bi- and trilayer h-BN due to interlayer coupling, providing a direct spectroscopic fingerprint of layer number and validating the layer-by-layer growth mode achieved by PA-MBE. Comparison with GW calculations further shows that the experimental spectra of bilayer and trilayer h-BN are consistent with polarized AB and ABA stacking configurations, respectively, while non-polarized stacking orders are excluded based on clear discrepancies in band dispersions. The spatial uniformity of band structures across different beam positions, together with second harmonic generation measurements, demonstrates homogeneous, millimeter-scale epitaxial growth with a polarized stacking configuration.

To elucidate the epitaxial growth mechanism, density functional theory calculations were performed to evaluate the formation energies of h-BN on graphene with various surface morphologies. Supported by high-resolution scanning transmission electron microscope imaging, the calculations show that graphene step edges, particularly concave regions, significantly lower the interfacial formation energy and serve as thermodynamically favorable nucleation sites. This step-guided conformal epitaxy accounts for the mono-oriented, polarized stacking of h-BN observed experimentally.

Furthermore, ferroelectricity in multilayer h-BN films was investigated using piezoresponse force microscopy (PFM) on Bernal-stacked graphene substrates. An OFF-field measurement protocol was employed to eliminate electrostatic artifacts and probe intrinsic polarization. Clear 180° phase reversals between bilayer and trilayer regions reveal layer-dependent polarization stacking driven by moiré and Bernal configurations. Applying a biased probe induces interlayer sliding, enabling reversible polarization switching characteristic of sliding ferroelectricity. Both bilayer and trilayer h-BN exhibit butterfly-shaped PFM amplitude loops and sharp phase switching at coercive voltages of ~±1.5 V, with trilayers showing the largest saturated response. Kelvin probe force microscopy confirms a stable ~300 meV surface potential contrast after switching, persisting for at least one week. Domain writing experiments demonstrate robust, damage-free polarization control, with trilayer h-BN offering superior uniformity and stability. These results establish epitaxial multilayer h-BN as a scalable, durable 2D ferroelectric platform. This work addresses key challenges in 2D ferroelectricity—scalability, stability, and switchability—by developing bottom-up, layer-by-layer epitaxial growth of hexagonal boron nitride (h-BN). A step-edge-guided process enables large-area, polar-stacked multilayer h-BN on h-BN/graphene moiré structures. As in graphene epitaxy, symmetry breaking at substrate steps is crucial for forming non-centrosymmetric van der Waals crystals. The resulting sliding ferroelectricity in h-BN, combined with the electronic, magnetic, and photonic properties of vdW materials, creates new opportunities for nonvolatile, reconfigurable 2D devices and multifunctional heterostructures. (Reported by Cheng-Maw Cheng)

*This report features the work of Chung-Ling Wu, Cheng-Maw Cheng and their collaborators published in Adv. Mater. **37**, 2414442 (2025).*

TLS 21B1 Angle-resolved UPS

- Angle-resolved Photoemission Spectroscopy
- Materials Science, Condensed-matter Physics

Reference

1. S.-S. Wong, Z.-Y. Lin, S.-Z. Ho, C.-E. Hsu, P.-H. Li, C.-Y. Chen, Y.-F. Huang, K.-E. Chang, Y.-C. Hsieh, C.-H. Chen, M.-H. Lee, M.-W. Chu, K.-I Lin, T.-M. Chen, Y.-C. Chen, H.-C. Hsueh, C.-M. Cheng, C.-L. Wu, Adv. Mater. **37**, 2414442 (2025).

Peeling Ferroelectrics to Power the Next Electronics Revolution

Freestanding ferroelectric membranes unlock CMOS-ready, low-power two-dimensional transistors and enable scalable logic for next-generation three-dimensional electronics.

As silicon-based complementary metal–oxide–semiconductor (CMOS) technology approaches its physical scaling limits, further transistor miniaturization faces increasing challenges such as heat dissipation and carrier mobility degradation. Two-dimensional (2D) semiconductors, with their atomically thin bodies and excellent electrostatic control, offer a promising alternative channel material for next-generation electronics. A critical bottleneck, however, is the integration of high-quality, high-κ gate dielectrics into 2D materials. Conventional atomic layer deposition often produces amorphous oxides and defective interfaces on 2D surfaces, while buffer-layer approaches can degrade dielectric performance. Although van der Waals insulators such as hexagonal boron nitride improve interfaces, their integration with CMOS processes remains difficult.

To overcome the barrier of integration with CMOS-compatible high-κ dielectrics, Jan-Chi Yang (National Cheng Kung University), Yen-Fu Lin (National Chung Hsing University), and their teams establish a reliable route to fabricate high-quality freestanding ferroelectric $Hf_{0.5}Zr_{0.5}O_2$ (HZO) membranes and systematically investigate their structural and electronic properties prior to integration with two-dimensional semiconductors. The freestanding HZO membranes are produced by selectively etching a sacrificial $La_{0.7}Sr_{0.3}MnO_3$ (LSMO) layer from epitaxial LSMO/HZO heterostructures grown on single-crystal $SrTiO_3$ substrates. They fabricated freestanding ferroelectric HfO_2-based oxides doped with zirconium (HZO) membranes using pulsed laser deposition and integrated with few-layer MoS_2 field-effect transistors (FETs). The membranes are produced by epitaxially growing an LSMO/HZO heterostructure on $SrTiO_3$, followed by selective chemical removal of the sacrificial LSMO layer. This approach yields mechanically intact membranes suitable for transfer without compromising crystallinity or ferroelectric functionality. Electrical characterization reveals that 20-nm-thick freestanding HZO membranes possess a high dielectric constant (~20.6), a large breakdown field (~2.2 MV cm^{-1}), and robust ferroelectric polarization.

High-resolution transmission electron microscopy reveals well-ordered atomic lattices in 20-nm-thick freestanding HZO membranes, dominated by the orthorhombic (o-) phase, which is responsible for ferroelectricity. Atomic force microscopy

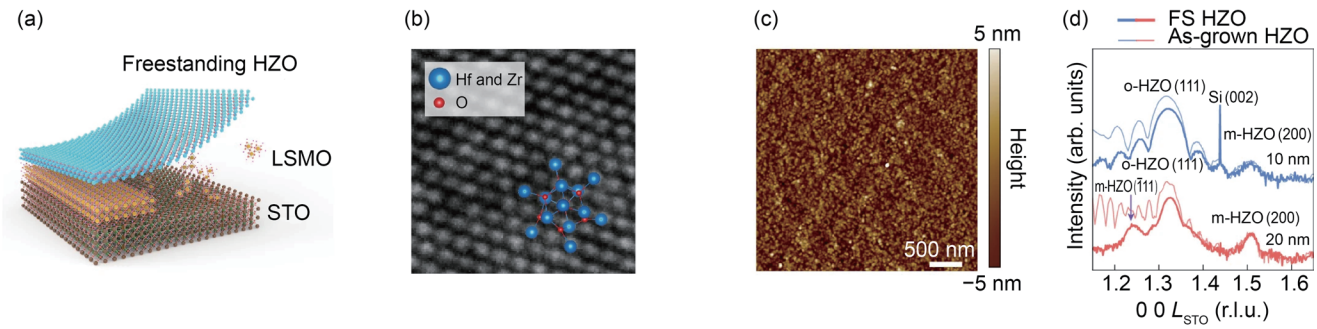

Fig. 1: Fabrication and characterization of ferroelectric freestanding HZO membranes. (a) Schematic of the fabrication process for freestanding HZO membranes. (b) Transmission electron microscopy image showing the o-phase (111) of freestanding HZO with the corresponding lattice model. (c) AFM image of a 20-nm freestanding HZO membrane, with an Ra value of 0.86 nm. (d) Comparison of XRD θ–2θ scans between as-grown and freestanding HZO membranes at thicknesses of 10 and 20 nm. [Reproduced from Ref. 1]

confirms smooth, crack-free surfaces, indicating that the release process preserves structural integrity. X-ray diffraction θ–2θ scans performed at **TPS 09A** and **TLS 13A1** comparing as-grown and freestanding HZO films (10–20 nm thick) show minimal changes in peak width and a slight high-angle shift, consistent with modest relaxation of in-plane compressive strain while maintaining high crystalline quality. Thickness-dependent X-ray diffraction (XRD) and off-normal measurements across films ranging from 5 to 40 nm further confirm excellent crystallinity and reveal a strong thickness dependence of phase composition. Notably, HZO films thinner than 20 nm exhibit an enhanced fraction of the ferroelectric o-phase, identifying them as optimal candidates for gate dielectrics.

To probe the connection between lattice symmetry and electronic structure, linear polarization-dependent X-ray absorption spectroscopy (XAS) was employed at **TPS 45A**. Oxygen K-edge spectra display clear linear dichroism arising from crystal-field-induced splitting of Hf (Zr) d states, enabled by the d^0 electronic configuration of Hf^{4+}/Zr^{4+}. Thick (~40 nm) HZO membranes show pronounced negative linear dichroism, characteristic of the centrosymmetric monoclinic phase. As membrane thickness decreases, the dichroism magnitude diminishes and reverses sign for sub-10-nm membranes, indicating a transition to a polar orthorhombic structure. This sign reversal provides direct spectroscopic evidence of polar lattice distortion and the emergence of ferroelectricity in ultrathin HZO membranes. Importantly, the linear dichroism trends of freestanding HZO closely match those of as-grown films, demonstrating that the freestanding process does not degrade structural or electronic quality. Together, these results confirm that ultrathin freestanding HZO membranes retain robust ferroelectricity and high crystallinity, providing a solid foundation for their integration as scalable, high-κ ferroelectric dielectrics in 2D electronic devices.

By transferring 20-nm-thick HZO membranes onto MoS_2, efficient top-gate control is achieved with a large capacitance of 0.44 μF cm^{-2}, corresponding to an equivalent oxide thickness of 4.5 nm. Analysis of the top- and bottom-gate coupling yields a dielectric constant of ~18.3, consistent with capacitance–voltage measurements. Crucially, carrier mobility remains comparable between SiO_2 bottom-gated and HZO top-gated devices, indicating that the freestanding membranes avoid charge doping and interface degradation typically associated with atomic layer deposition. Statistical measurements from 32 devices show excellent uniformity, with over 65% achieving on/off current ratios near 10^8 and an average subthreshold swing of 53 mV dec^{-1}. Moreover, the ferroelectric nature of HZO ensures efficient gate control and stable switching behavior. Using these devices, functional logic components such as inverters, logic gates, and a 1-bit full adder are demonstrated. In addition, short-channel MoS_2 transistors with channel lengths down to 13 nm maintain excellent performance, highlighting the scalability of this approach. The researchers' work establishes freestanding ferroelectric HZO membranes as a viable pathway for integrating high-κ dielectrics with 2D semiconductors for advanced, CMOS-compatible electronics.

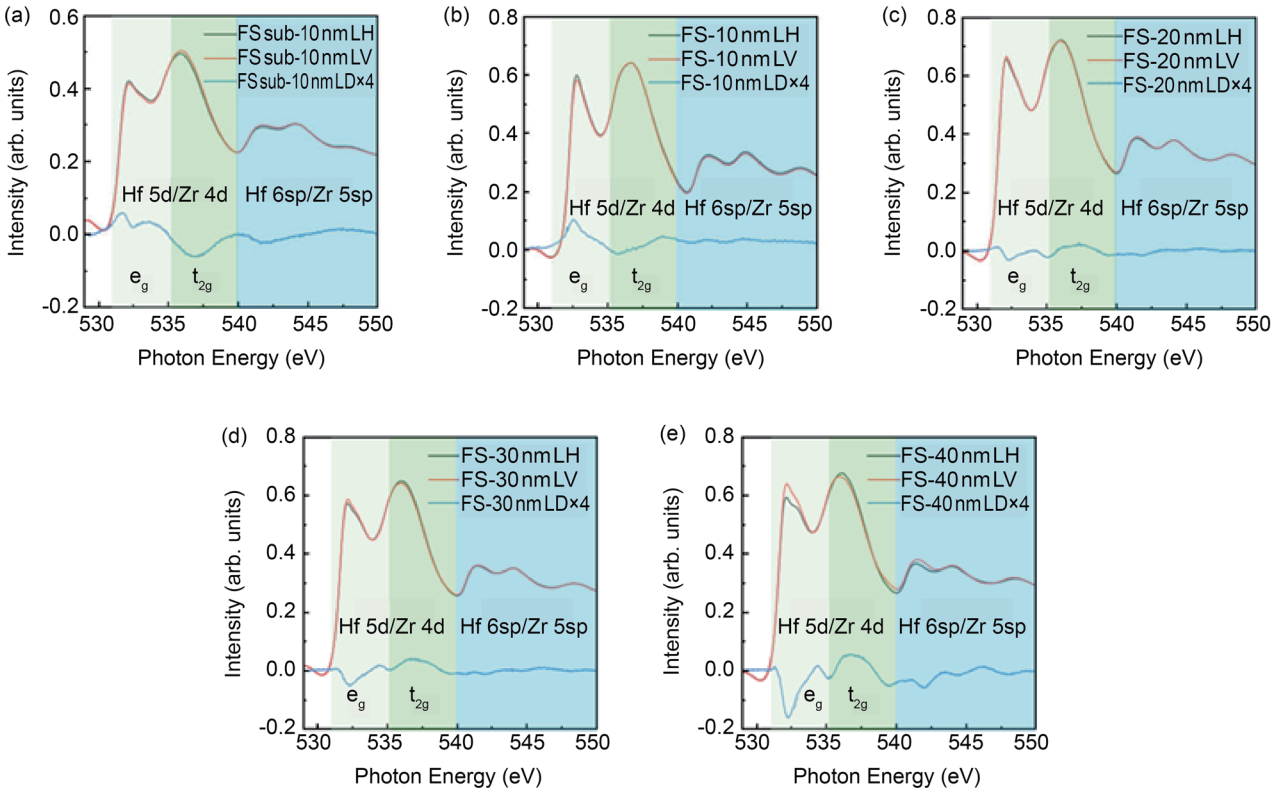

Fig. 2: Thickness-dependent XAS and XLS spectra of freestanding HZO membranes. [Reproduced from Ref. 1]

In summary, this work demonstrates freestanding high-κ ferroelectric HZO membranes grown by pulsed laser deposition and transferred onto 2D semiconductors to enable high-performance MoS_2 FETs. Owing to strong ferroelectricity, a dielectric constant of ~20.6, and an excellent interface quality (Dit ≈ 9×10^{10} cm^{-2} eV^{-1}), the devices achieve Ion/Ioff ≈ 10^9 and a minimum subthreshold swing of 53 mV dec^{-1}. Integrated logic circuits and scalable short-channel operation highlight HZO membranes as a CMOS-compatible dielectric platform for advanced 2D and 3D integrated electronics. (Reported by Cheng-Maw Cheng)

This report features the work of Jan-Chi Yang, Yen-Fu Lin and their collaborators published in Nat. Electron. ***8****, 560 (2025).*

TPS 09A Temporally Coherent X-ray Diffraction
TPS 45A Submicron Soft X-ray Spectroscopy
TLS 13A1 X-ray Scattering

- Soft-X-ray absorption spectroscopy, X-ray diffraction
- Materials Science, Condensed-matter Physics

Reference

1. C.-Y. Lin, B.-C. Chen, Y.-C. Liu, S.-F. Kuo, H.-C. Tsai, Y.-M. Chang, C.-Y. Kuo, C.-F. Chang, J.-H. Chen, Y.-H. Chu, M. Yamamoto, C.-H. Shen, Y.-L. Chueh, P.-W. Chiu, Y.-C. Chen, J.-C. Yang, Y.-F. Lin, Nat. Electron. **8**, 560 (2025).

An "*s*-Electron" Donor Band Drives the Metallic Ferromagnetism in Co-Doped ZnO Films

Polarization-dependent, bulk-sensitive hard X-ray photoemission spectroscopy reveals that a metallic "s-electron" character donor band mediates ferromagnetism in Co-doped ZnO films and solves a long-standing problem in dilute magnetic materials.

Diluted magnetic semiconductors (DMSs) hold great potential for spintronic applications and continue to attract significant attention as room-temperature ferromagnetic (RTFM) materials. While doping transition metals (TMs) into oxide semiconductors is a common approach, the underlying physical mechanism remains poorly understood, particularly for the diluted magnetic oxide (DMO) Co-doped ZnO (Co:ZnO) films, which exhibit high Curie temperatures (T_C) exceeding 300 K. The most promising mechanism proposed for high-T_C ferromagnetism is the donor impurity band exchange model, in which donor electrons mediate the coupling between TM spins. However, the nature of the donor band electrons has not yet been identified experimentally. Based on a well-planned set of experiments, including material synthesis, magnetic measurements, X-ray absorption near-edge and extended X-ray absorption fine-structure spectroscopy (XANES, EXAFS), and polarization-dependent, bulk-sensitive hard X-ray photoemission spectroscopy (HAXPES), Jung-Chun-Andrew Huang (National Cheng Kung University) and his collaborators have now demonstrated that the donor band originates in $Zn^{1+}4s^1$ states in Co:ZnO epitaxial films.[1] The study provides new insight into the ferromagnetic mechanism in Co:ZnO, where $Zn^{1+}4s^1$ states mediate ferromagnetism, leading to Co^{2+} spin ordering and metallic-like transport. These results elucidate the complementary roles of dopant and host electronic states and open avenues for designing novel room-temperature DMSs.

It is well-known from the donor impurity band exchange mechanism proposed by Coey *et al.*[2] that hybridization between TM states and defects influences the magnetic and electrical properties of DMOs. In ZnO-based DMOs, impurity bands arising from defects or TM 3*d* states can behave as localized states at low density and retain semiconducting behavior, or they can broaden with increased defect density and exhibit metallic transport. Accordingly, the authors first developed fabrication methods that preserve structural defects in the films. Epitaxial Co-doped ZnO films were grown using radio-frequency magnetron sputtering (RF sputtering) on sapphire substrates, maintaining a low Co doping concentration (~5 at%) to avoid percolation effects. The films were carefully optimized to preserve structural defects, such as zinc interstitials and oxygen vacancies. For a comparative analysis, four sets of samples were prepared

on Al_2O_3 (0001) substrates by RF sputtering in this study. The concentration of oxygen vacancies was controlled by varying the H2 content mixed with Ar during deposition. Samples A and B contained 5 at% Co doping in a 40 nm Co:ZnO layer. The H_2/Ar ratios during sputtering were 5% for sample A and 2.5% for sample B. After deposition, both samples were capped with a 2 nm ZnO protective layer with no H_2 exposure during sputtering. Sample C was structurally identical to sample A but lacked the ZnO protective layer. These samples facilitate the investigation of the presence and absence of defects, such as oxygen vacancies, while eliminating charging effects during HAXPES measurements and thereby enable a reliable comparison of their relationship with variation in magnetic properties. In addition, to compare the effects of Co doping on ZnO, a highly conductive ZnO film (40 nm) was prepared, denoted as sample D, using a 2.5% H_2/Ar ratio during growth. The growth parameters of samples A, B, C, and D are summarized in **Table 1**.

Table 1: Growth parameters for samples A, B, C, and D.

	Capping Layer	Main Layer	H_2/Ar Ratio during Sputtering
Sample A	2 nm ZnO	40 nm Co (5 at%):ZnO	5%
Sample B	2 nm ZnO	40 nm Co (5 at%):ZnO	2.5%
Sample C	none	40 nm Co (5 at%):ZnO	5%
Sample D	none	40 nm ZnO	2.5%

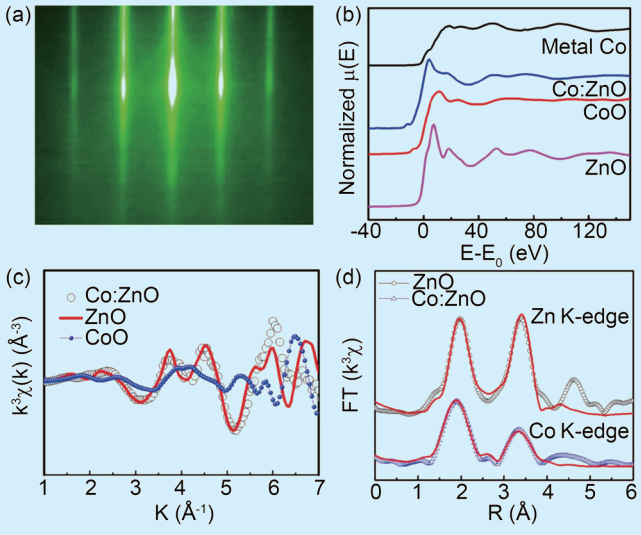

Fig. 1: (a) RHEED pattern of the $Co_{0.05}Zn_{0.95}O$ film along the [11-20] azimuth, indicating high crystallinity. (b) Normalized XANES spectra at the Zn K-edge for undoped ZnO (sample D) and at the Co K-edge for Co (5 at%)-doped ZnO (sample A), compared with reference spectra from CoO powder and Co metal foil. (c) k^3-weighted χ(k) functions at the Zn K-edge (ZnO) and Co K-edge (Co:ZnO), with CoO as reference. (d) Fourier transformed EXAFS spectra of Co:ZnO at the Co K-edge and ZnO at the Zn K-edge. The overlaid fitting curve for Co:ZnO shows a local structural environment closely resembling that of Zn in ZnO. [Reproduced from Ref. 1]

The epitaxial films were characterized by reflection high-energy electron diffraction (RHEED), as shown for one case in **Fig. 1(a)**. XANES experiments at Taiwan-contract beamline BL12B2 in SPring-8 [**SP 12B1**](**Fig. 1(b)**) were conducted to confirm that the Co atoms exhibit divalent Co^{2+} spectral features by comparison with a reference CoO sample. This was also confirmed by the HAXPES Co 2*p* spectrum and configuration interaction cluster model calculations. The authors then performed EXAFS measurements for the Co:ZnO samples, CoO, and ZnO. The data were analyzed using Fourier-transformed EXAFS spectra for all samples to demonstrate that the doped Co atoms occupy the Zn sites in the Co:ZnO epitaxial films, as shown in **Figs. 1(c) and 1(d)**.

Magnetization (M) versus magnetic field (H) measured at room temperature for H in the in-plane direction is shown in **Fig. 2**, confirming clear ferromagnetism in the Co:ZnO samples with a protective layer. The M–H hysteresis loops for samples A and B reveal saturation magnetization (M_S) values of approximately 1.09 and 0.38 μ_B/Co, respectively, as shown in **Fig. 2**. In contrast, the M_S values of sample C and sample D (ZnO) are very small, less than 0.05 μ_B/Co. These findings indicate the crucial role of both magnetic doping and structural defects in achieving RTFM in Co:ZnO. Furthermore, the magnetic properties of Co:ZnO without the protective layer (sample C) were monitored over time by exposing the samples to ambient conditions. The results indicated a monotonic decay in the ferromagnetic signal over time, reinforcing the critical role of both magnetic doping and structural defects in obtaining RTFM in Co:ZnO. Although similar findings have been reported in the literature, direct evidence for the presence of an impurity band in defect-protected Co:ZnO was not provided in earlier studies.

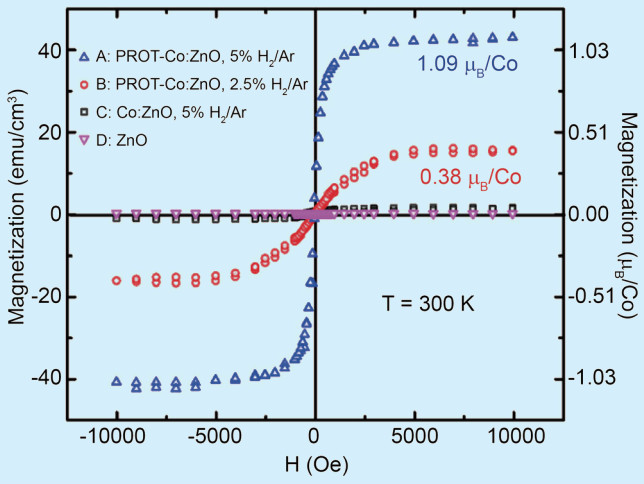

Fig. 2: Magnetization of samples A, B, C, and D at room temperature. The data have been corrected for the linear diamagnetic contribution of the sapphire substrates. [Reproduced from Ref. 1]

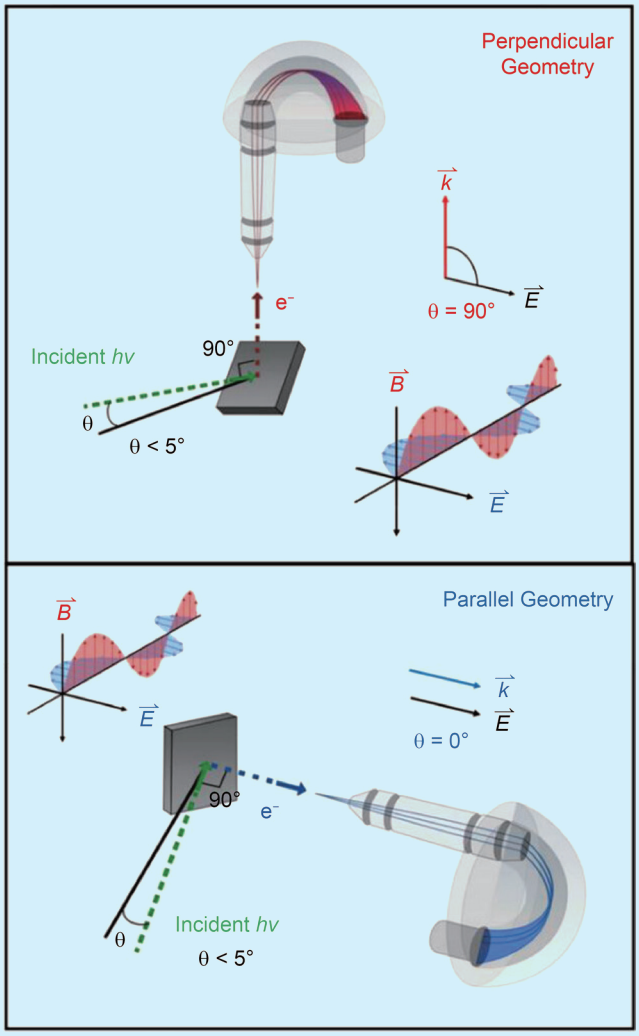

Fig. 3: Experimental geometry of the polarization dependent HAXPES setup is defined by the angle θ between the incident photon beam electric field vector $\vec{E}$ and the momentum $\vec{K}$ of photoemitted electrons. The incident photon beam is linearly polarized with the electric field vector within the horizontal plane of the synchrotron ring. Top: In the perpendicular polarized geometry (also called s-polarized, where s stands for senkrecht≡perpendicular, in German), we use a vertically mounted analyzer, θ = 90°, and then $\vec{K}$ is perpendicular to $\vec{E}$. Bottom: In the parallel geometry, also called the p-polarized geometry, we use a horizontally mounted analyzer, θ = 0°, and $\vec{K}$ is parallel to $\vec{E}$. Then, based on the angular dependence of differential ionization cross-sections, one can distinguish features due to s-, p-, d-,...type photoemitted electrons in a sample from the measured spectral intensities in the parallel and perpendicular geometries. [Reproduced from Ref. 1]

A key advantage of using HAXPES experiments with high incident photon energy is the enhanced probing depth, which enables the access to the intrinsic bulk electronic structure. Most importantly, polarization-dependent HAXPES can resolve the orbital character of electronic states in the valence band. Accordingly, polarization-dependent HAXPES measurements were performed at the Taiwan-contract beamline BL12XU in SPring-8, Japan [**SP 12U1**]. The experimental setup enables independent detection of photoelectrons with momentum components both perpendicular and parallel to the electric field of nearly grazing incidence (< 2°) synchrotron light, as schematically illustrated in **Fig. 3**.[3,4] The authors first conducted polarization-dependent HAXPES of the O 1*s*, Co 2*p*, and Zn 2*p* core levels of Co:ZnO samples. After normalizing the spectra to the Zn 2*p*3/2 core level main peaks, the results confirmed that the O 1*s* spectra, with a main peak at 530.36 eV and a weaker feature at 531.34 eV, showed clear polarization dependence with significantly higher intensity in the parallel geometry compared to the perpendicular geometry. In contrast, the Co 2*p* peaks did not show evidence of polarization dependence, while the results confirmed that the Co ions are divalent Co^{2+}.

Next, the authors measured the HAXPES data for the parallel and perpendicular geometries within 6 eV BE for samples A–D, as shown in **Figs. 4(a) and 4(b)** on the next page. The results revealed a band at approximately 2.7 eV but with significantly different spectral intensities. The spectral intensity of this feature showed the same trend in both geometries; it is maximum for sample A and decreases for sample B and gets further reduced for sample C, while the feature is totally missing in sample D, it follows the magnetization magnitude of the samples and indicates that the 2.7 eV BE feature is due to Co 3*d* states. Note that although sample B exhibited a lower defect concentration (H_2/Ar ratio of 2.5%), it was protected by a capping layer, whereas sample C, with a higher defect concentration (H_2/Ar ratio of 5%), remained uncapped. Since the long-range ordered high-T_C samples A and B are nearly metallic, the authors conducted a high signal-to-noise ratio examination of the HAXPES data at and near E_F to check for the donor band, as shown in **Figs. 4(c) and 4(d)**. For samples A–C shown in **Fig. 4(c)**, the data reveal a band peaked at around 0.3 eV below E_F in samples A and B and crosses E_F with finite intensity; however, this feature is absent in sample C. More importantly, the 0.3 eV peak is strongly suppressed in the perpendicular geometry for samples A and B. It is important to note that the HAXPES signal associated with Zn 4*s* orbitals is reduced by the polarization factor in the perpendicular geometry. Thus, the magnitude of its spectral weight reduction, combined with the absence of the feature in sample C—which includes Co 3*d* states at 2.7 eV BE, as seen in **Figs. 4(a) and 4(b)**—indicates that the 0.3 eV feature originates from a predominantly Zn 4*s* character metallic donor band, as measured by HAXPES. Finally, to validate the Zn 4*s* character of the donor band, we measured the polarization dependence of sample D, as shown in **Fig. 4(d)**. The results reveal an electron donor band even for sample D. While it is weaker than the donor bands observed in samples A and B, it shows qualitatively similar polarization dependence, with strongly suppressed spectral intensity in the perpendicular geometry, akin to the electron donor bands seen in Co-doped ferromagnetic samples A and B. Since sample D does not contain Co 3*d*

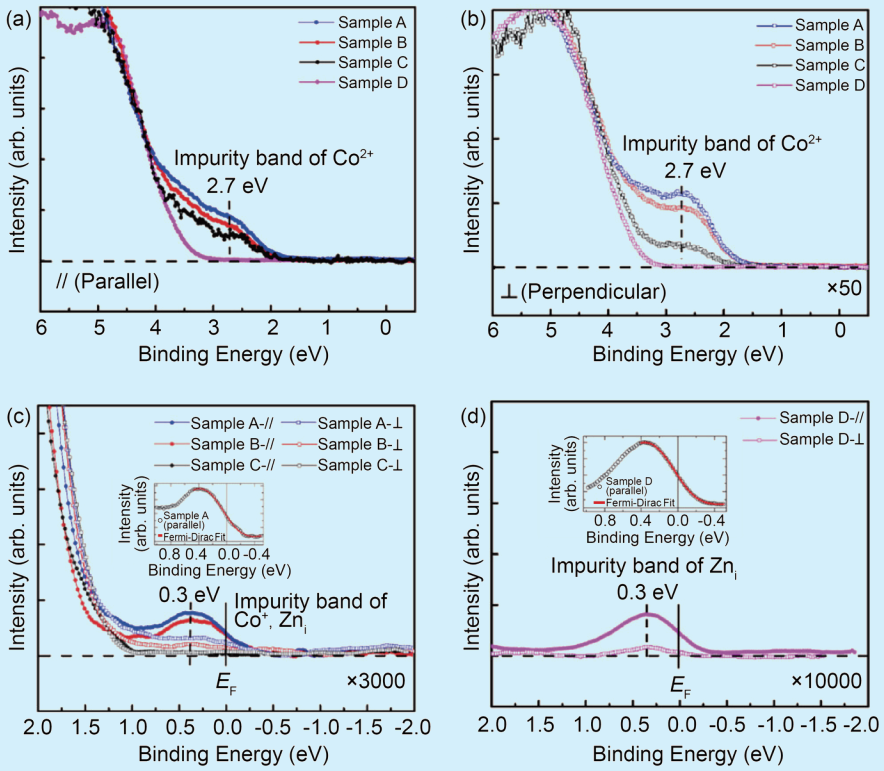

Fig. 4: (a) Valence band HAXPES spectrum measured in parallel geometry, serving as the reference for the y-axis scale across all panels in this figure. (b) Magnified view (×50) relative to the y-axis scale of (a), showing the valence band HAXPES spectrum acquired under the perpendicular geometry. (c) Highly magnified view (×3000) relative to the y-axis scale of (a), comparing the valence band HAXPES spectra of samples A, B, and C measured in the parallel and perpendicular geometries. Inset: Fermi edge observed in sample A in the parallel geometry. (d) Further magnified view (×10000) relative to the y-axis scale of (a), displaying the valence band HAXPES spectra of sample D in parallel and perpendicular geometries. Inset: Fermi edge observed in sample D in parallel geometry. [Reproduced from Ref. 1]

dopants, this result unambiguously indicates that the donor band originates from Zn 4*s* character electrons.

The authors conclude that polarization-dependent HAXPES measurements provide direct evidence of an impurity donor band in Co-doped ZnO, characterized by a Zn 4*s* metallic band crossing the Fermi level. This supports the Ruderman-Kittel-Kasuya-Yosida model for high-T_C ferromagnetism in Co-doped ZnO. This finding offers new insights into the ferromagnetic mechanism, wherein $Zn^{1+}4s^1$ states mediate ferromagnetism in Co-doped ZnO. (Reported by Ashish Chainani)

This report features the work of Jung-Chun-Andrew Huang and his collaborators published in Adv. Sci. ***12****, e08148 (2025).*

SP 12B1 Materials X-ray Study
SP 12U1 Hard X-ray Photoelectron Spectroscopy

- XANES, EXAFS, HAXPES
- Materials Science, Condensed-matter Physics

References

1. P.-Y. Chuang, J.-C. A. Huang, A. Chainani, H.-S. Hsu, Y.-F. Liao, C.-Y. Sung, C.-H. Liu, C.-Y. Liao, C.-H. Lee, K.-D. Tsuei, Adv. Sci. **12**, e08148 (2025).
2. J. M. D. Coey, M. Venkatesan, C. B. Fitzgerald, Nat. Mater. **4**, 173 (2005).
3. J. Weinen, A. Fiedler, M. Merkel, D. Flahaut, S. Cramm, B. Ruck, J. Electron Spectrosc. Relat. Phenom. **198**, 6 (2015).
4. F. Offi, G. Panaccione, A. Fondacaro, P. Torelli, N. B. Brookes, G. Rossi, Nucl. Instrum. Methods Phys. Res. A **550**, 454 (2005).